

# Iron self-diffusion in FeZr/ $^{57}\text{Fe}$ Zr multilayers measured by neutron reflectometry: Effect of applied compressive stress

Mukul Gupta<sup>1,2\*</sup> and Ajay Gupta<sup>1</sup>, Sujoy Chakravarty<sup>1</sup>, Rachana Gupta<sup>1,2</sup> and Thomas Guterlet<sup>2</sup>

<sup>1</sup>UGC-DAE Consortium for Scientific Research, Khandwa Road, Indore, 452017, India

<sup>2</sup>Laboratory for Neutron Scattering, ETH Zürich and Paul Scherrer Institute, CH-5232 Villigen PSI, Switzerland

(Dated: September 6, 2018)

Iron self-diffusion in nano-composite FeZr alloy has been investigated using neutron reflectometry technique as a function of applied compressive stress. A composite target of Fe+Zr and  $^{57}\text{Fe}$ +Zr was alternatively sputtered to deposit chemically homogeneous multilayer (CHM) structure, [ $^{nat}\text{Fe}_{75}\text{Zr}_{25}/^{57}\text{Fe}_{75}\text{Zr}_{25}$ ]<sub>10</sub>. The multilayers were deposited on to a bent Si wafer using a 3-point bending device. Post-deposition, the bending of the substrate was released which results in an applied compressive stress on to the multilayer. In the as-deposited state, the alloy multilayer forms an amorphous phase, which crystallizes into a nano-composite phase when heated at 373 K. Bragg peaks due to isotopic contrast were observed from CHM, when measured by neutron reflectivity, while x-ray reflectivity showed a pattern corresponding to a single layer. Self-diffusion of iron was measured with the decay of the intensities at the Bragg peaks in the neutron reflectivity pattern after thermal annealing at different temperatures. It was found that the self-diffusion of iron slows down with an increase in the strength of applied compressive stress.

PACS numbers: 66.30.Fq

## I. INTRODUCTION

During recent decades amorphous and nanocrystalline metals and alloys have been investigated as an important class of materials with the possibility of tailoring their properties over a wide range by controlling particle size and morphology.<sup>1,2,3,4</sup> More recently nano-composite alloys, in which nanocrystals are surrounded by an intergranular amorphous matrix, have attracted a great attention due to their interesting structural<sup>5</sup> and magnetic properties.<sup>6,7,8</sup> One of the favorable way to obtain a nano-composite alloy, is partial crystallization of the amorphous alloy.<sup>2,9,10</sup> The alloy structure obtained above the primary crystallization temperature of the parent amorphous phase, but below the secondary crystallization temperature, has been termed as nano-composite phase.<sup>11</sup> Above the secondary crystallization temperature, the nano-composite structure fully crystallizes to form an equilibrium state of the alloy. Structurally, the nanocrystals obtained after primary crystallization are surrounded by an amorphous inter-granular phase to form a nano-composite phase.<sup>1,12</sup> Nano-composite alloys produced with an amorphous precursor are the basis of interesting soft-magnetic alloys known as FINEMET<sup>13</sup>, NANOPERM<sup>14</sup>, HITPERM<sup>15</sup>. Since the nano-composite phases produced in these alloys is inherently a metastable phase, diffusion of the constituents would play an important role in understanding and determining their properties for long-standing applications. Hence, atomic diffusion in such alloys is the key phenomenon for selecting their applications.<sup>16</sup>

The situation becomes more complicated when the nano-composite alloys are produced in the form of a thin film. Deposition of thin films on to a substrate is known to produce films with a large intrinsic strain or stresses which often results from differences in thermal expansion

(thermal stress) or from the microstructure of the deposited film (intrinsic stress).<sup>17,18,19</sup> The intrinsic stresses may originate due to several factors (i) at the strained regions within the films e.g. grain-boundaries, dislocations, voids, impurities, etc. (ii) at the film/substrate interface due to lattice mismatch, different thermal expansion, etc. (iii) at the film/vacuum interfaces due to surface stress, adsorption, etc. or (iv) due to a dynamic processes e.g. re-crystallization, interdiffusion, etc.<sup>20</sup> These stresses may significantly affect the physical properties of the thin films, including atomic diffusion.

It is known that when a material is deposited in the thin film state, the diffusion mechanism can be completely different as compared to bulk state of that material, even when the material is in purely elemental form. Such a behavior has been mainly attributed to an increased defect concentration, metastability and unrelaxed state of the material. Therefore an extrapolation of bulk diffusivity may results in erroneous values of diffusivity in the case of thin films. Since many devices which are used for application are fabricated in the form of nm range thin films, self-diffusion measurements can be extremely important for their applications.

In order to study the nature of stresses on self-diffusion we have chosen a simple binary FeZr alloy for this purpose. It was found that (as will be shown later) after annealing at 373 K, the alloy forms a nano-composite phase which further crystallizes above 600 K. The self-diffusion of iron was measured in the nano-composite state as a function of applied stress. The samples were deposited on to a substrate with a known bending. An external stress on to an [ $^{nat}\text{Fe}_{75}\text{Zr}_{25}/^{57}\text{Fe}_{75}\text{Zr}_{25}$ ]<sub>10</sub> multilayer was applied by releasing the bending of the substrate which resulted in an applied compressive stress on to the sample. Iron self-diffusion measurements were carried out using neutron reflectivity technique. It may be

noted that the neutron reflectivity is an excellent technique for studying self-diffusion in nm range structures. Due to the fact that neutron scattering length densities for isotopes of an element are different, neutron reflectivity with depth resolution in sub nm range provides a unique opportunity for measuring self-diffusion. Conventional cross-sectioning and depth-profiling techniques, such as radiotracer, secondary ion mass spectroscopy (SIMS) are not suitable for measuring self-diffusion in nm range structures as the depth resolution available with cross-sectioning and depth-profiling techniques is of the order of a few nm.

In an earlier work<sup>21</sup> we have demonstrated that neutron reflectivity is a technique which could be used to probe diffusion lengths of the order of 0.1 nm, and diffusion at temperatures less than 400 K could be measured. In the present work, the effect of compressive stress on the self-diffusion of iron in nano-composite multilayers was studied using neutron reflectivity.

## II. SAMPLE PREPARATION AND CHARACTERIZATION

FeZr, CHM have been deposited on Si (100) substrates using magnetron sputtering technique. Small pieces of Zr rods were pasted on the <sup>natural</sup>Fe and <sup>57</sup>Fe targets in a symmetric way and the composite targets were sputtered alternately to prepare a chemically homogeneous structure with nominal a composition Si/[<sup>natural</sup>Fe<sub>75</sub>Zr<sub>25</sub> (25 nm)/<sup>57</sup>Fe<sub>75</sub>Zr<sub>25</sub> (10 nm)]<sub>10</sub>. The deposition of the multilayer was carried out after obtaining a base pressure better than  $1 \times 10^{-6}$  mbar. During the deposition, pressure in the chamber was  $5 \times 10^{-3}$  mbar due to 30 cm<sup>3</sup>/min Ar gas flow used for sputtering of the targets. All the samples were deposited at a constant sputtering power of 50 W. Before deposition the vacuum chamber was repeatedly flushed with Ar gas so as to minimize the contamination of the remaining gases present in the chamber. Both the targets were pre-sputtered at least for 10 min. During the deposition the substrate was mounted on a specially designed 3-point Si wafer bending device. The substrate was oscillated with respect to central position of the target for better uniformity of the thickness of the deposited sample.

In all the cases, thin Si wafers ( $300 \pm 10$ )  $\mu\text{m}$  were used as a substrate in order to avoid breaking during bending. The Si wafer was fixed from both the ends, and by rotation of an asymmetric roller around the central axis, the bending height of the Si wafer can be varied between 0 to 5 mm. A pin-lock system was incorporated so that release of bending by itself could be avoided. A compressive stress is applied on to the deposited film, when the bending of the Si wafer was released after deposition. The applied stress due to release of bending on to the Si wafer can be calculated using Stoney's formula<sup>22</sup> and following a discussion given by Chen et al.<sup>23</sup> The applied

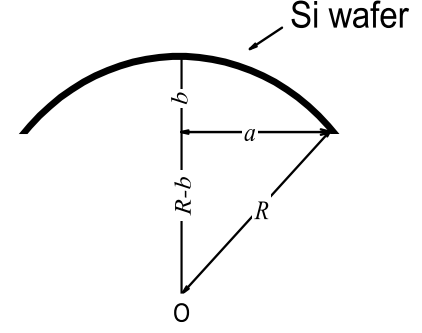


FIG. 1: Schematic diagram of the bent Si wafer, used for calculation of radius of curvature.

stress  $\sigma$ , is given by:

$$\sigma = \frac{\left(\frac{E_{Si}}{1-\nu_{Si}}\right)T_{Si}^2}{6RT_f}, \quad (1)$$

Where  $\left(\frac{E_{Si}}{1-\nu_{Si}}\right)$  is the biaxial modulus of the silicon substrate and is equal to 180.5 GPa.  $E_{Si}$  is Young's modulus for Si and  $\nu_{Si}$  is Poisson's ratio for Si.  $T_{Si}$  is the thickness of the substrate,  $T_f$  is the thickness of the film and  $R$  is the radius of curvature. With the situation shown in the fig. 1, the radius of curvature can be written as:

$$R = \frac{a^2 + b^2}{2b}, \quad (2)$$

Combining equation (1) and (2), the value of stress was calculated. The parameter used in the present case are  $T_{Si} = (300 \pm 10) \mu\text{m}$ ,  $T_f = 370$  nm,  $a = 40$  mm and  $b$  was varied at 0, 3 and 5 mm. The obtained values of stress for the 3 cases are 0, 27 and 46 GPa. The errors in the calculation of applied stress were of the order of 15-20%, taking into account the uncertainties in the measured physical parameters. Samples with different known bending were deposited under similar deposition conditions. After deposition and release of bending, the surface profile of the samples was measured using a profilometer. It was found that the surface of the samples was flat and no changes in the surface profile were observed for a sample prepared with or without bending. This indicated that even after the bending the substrate gains its original state and the stress is applied on to the deposited multilayer.

The composition of the deposited films was determined using x-ray photoelectron spectroscopy (XPS) depth profiling. The XPS profile was measured using monochromatic Al  $K_{\alpha}$  x-rays (1mm spot size) at the surface and at 3 different depths, after sputtering with Ar ions of 1 mA current and 3 kV accelerating voltage. The pressure during measurements was better than  $1 \times 10^{-8}$

mbar. The average composition of the films was equal to  $\text{Fe}_{75\pm3}\text{Zr}_{25\pm3}$ , excluding the data taken at the surface. Since at the surface, contributions from adsorbed species like carbon and oxygen were significant, the average composition of the film was determined with the data taken at 3 different depths. A small amount of oxygen was detected throughout the depth of the film.

Structural characterizations of the samples were carried out with x-ray reflectivity (XRR) and grazing incidence diffraction using a standard x-ray diffractometer (XRD) with  $\text{Cu-K}\alpha$  x-rays. The crystallization behavior of the multilayers was examined using differential scanning calorimetry (DSC) with NETZSCH, DSC equipped with extremely high sensitivity  $\mu$ -Sensor. The conversion electron Mössbauer spectroscopy measurements (CEMS) were performed for determining the local environment of  $^{57}\text{Fe}$  in the samples. The measurements were carried out using a 50 mCi  $^{57}\text{Co}$ -radioactive source in a Rh matrix and a gas flow proportional counter ( $\text{He}+4\%\text{CH}_4$ ) for detection of conversion electrons. The isomer shifts were calibrated relative to  $\alpha$ -Fe. Hysteresis loops as a function of azimuthal angle were measured using magneto optical Kerr effect (MOKE).

Self-diffusion measurements were performed using neutron reflectometry technique at AMOR reflectometer at the Swiss spallation neutron source (SINQ), at Paul Scherrer Institute, Switzerland.<sup>24</sup> The reflectivity pattern was measured using two different angular settings ( $0.5^\circ$  and  $1.0^\circ$ ) in the time-of-flight mode.

### III. RESULTS AND DISCUSSION

#### A. Structural Properties

The multilayers prepared in this work have a periodicity only for iron isotopes, it is expected that x-ray reflectivity of the multilayers would show a pattern corresponding to a single layer. Fig. 2 shows x-ray reflectivity pattern of the multilayer structure prepared at 0, 27 and 46 GPa. As can be seen from the pattern, at the designed period of the multilayer there was no contrast for x-rays, which confirms the chemical homogeneity of the layers. The x-ray reflectivity pattern was fitted assuming a single layer and an ‘oxide’ layer of about 6 nm thickness on the surface of the multilayer, using a computer program based on Parratt’s formalism.<sup>25</sup> Such an oxide layer on the surface of the sample may stem because of absorbed oxygen or other light elements, when the samples are exposed to the atmosphere after deposition. Presence of such a layer was also evident from XPS measurements.

On the other hand the neutron reflectivity pattern (fig. 3), showed well-pronounced Bragg peaks arising due to isotopic contrast between  $^{nat}\text{Fe}$  and  $^{57}\text{Fe}$ . As can be seen from the figure, the sample prepared without any stress showed rather asymmetric Bragg peaks, while for the samples prepared with an applied stress, the peaks were more symmetric. Such an asymmetry of the Bragg

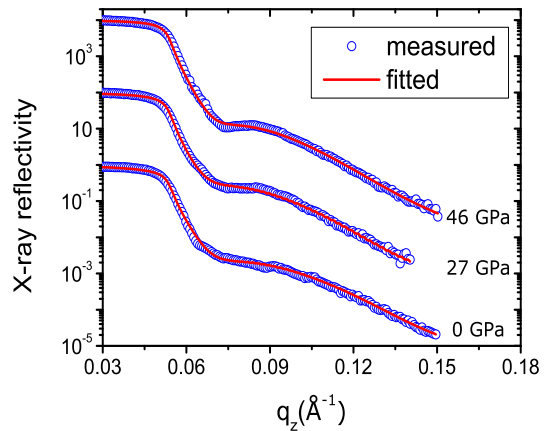


FIG. 2: (color online) X-ray reflectivity of the as-deposited  $\text{Si}/[^{nat}\text{Fe}_{75}\text{Zr}_{25} (25\pm1 \text{ nm})/^{57}\text{Fe}_{75}\text{Zr}_{25} (12\pm1 \text{ nm})]_{10}$  multilayer at different applied stresses. The intensity shown on y-axis has been multiplied by a factor of 100, for clarity.

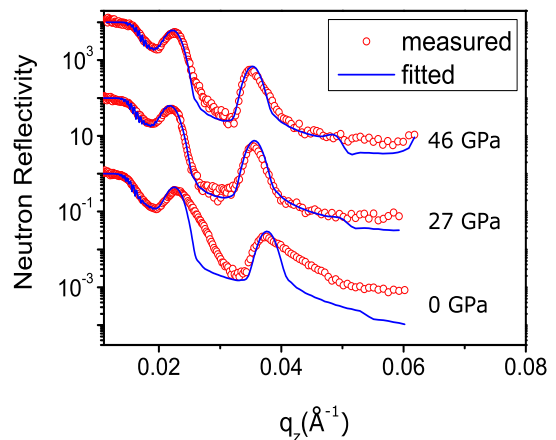


FIG. 3: (color online) Neutron reflectivity of the as-deposited  $\text{Si}/[^{nat}\text{Fe}_{75}\text{Zr}_{25} (25\pm1 \text{ nm})/^{57}\text{Fe}_{75}\text{Zr}_{25} (12\pm1 \text{ nm})]_{10}$  multilayer prepared with applied stresses of 0, 27 and 46 GPa. The intensity shown on y-axis has been multiplied by a factor of 100, for clarity.

peaks may arise due to incorporation of some free volume which may result in some internal strain or stresses during the growth of the film and might cause an asymmetry in the scattering length density. For the samples which were prepared in the bent state, the release of bending results into an applied external stress on to the multilayer which eventually results in annihilation of free volume. A more detailed discussion related to this issue is given in the next sections.

The neutron reflectivity pattern was fitted using a computer program based on Parratt’s formalism<sup>25</sup> and it was found that the pattern could not be fitted assuming sharp interfaces; instead a thin inter-layer of thickness  $(1\pm0.5)$  nm with the mean scattering length density of the two layers had to be introduced as inter-diffused layer. This means that already at room temperature

there is some amount of interdiffusion in the multilayer. The fitted parameters gives the structure of the multilayers:  $\text{Si}/[\text{natural Fe}_{75}\text{Zr}_{25} (25\pm 1 \text{ nm})/^{57}\text{Fe}_{75}\text{Zr}_{25}(12\pm 1 \text{ nm})]_{10}$ , which is close to the nominal structure.

## B. Crystallization Behavior

Prior to diffusion measurements thermal stability of the samples was studied with grazing incidence x-ray diffraction. All the samples were annealed together in a vacuum furnace in the temperature range of 373-573 K with 100 K step. In the as-prepared state all the samples show a diffuse maxima centered around  $2\theta = 44.6^\circ$ , with a width of about  $4\text{-}5^\circ$  (see Fig. 4), which means that the samples are x-ray amorphous in the as-prepared state. The width of the diffuse maxima is comparable to the iron based amorphous alloys.<sup>2</sup> The average inter-atomic distance can be estimated using the relation,<sup>26</sup>  $a = 1.23\lambda/2\sin\theta$ , where  $\theta$  is taken to be the angle at the center of the diffuse maxima, and the factor 1.23 is a geometric factor which rationalizes the nearest neighbor distance with the spacing between ‘pseudo-close packed planes’. As shown in the fig. 4, with an increase in the applied stress the position of the amorphous maxima shifts towards higher angle side indicating a decrease in the average inter-atomic distance as shown in the inset of the figure. Such a decrease in the average inter-atomic distance may be caused due to applied compressive stress. After annealing at 373 K, the broad hump becomes narrow (width  $\sim 1^\circ$ ) and a nano-composite structure is found, as shown in fig. 5. The peak shape from the nano-composite structure could be fitted only by deconvoluting it into two lines, one corresponding to the parent amorphous phase and the second to a nanocrystalline bcc-Fe phase. The area ratio of amorphous phase as determined from the fitting of XRD data was in the range of 15-25%. A slight decrease in the area ratio of the amorphous phase was observed. On further annealing at 473 and 573 K, no significant changes in the XRD pattern of the samples were observed as shown in fig. 5. After annealing at different temperatures the position of Bragg peak shifts towards higher angle indicating a further decrease in the interatomic spacing. Such a decrease in interatomic spacing is related with structural relaxation and is a consequence of annihilation of free volume. The grain size of the nanocrystals was about 10 nm, which increases marginally with an increase in the annealing temperature as shown in fig. 6.

Crystallization behavior of the samples was also studied using conversion electron Mössbauer spectroscopy (CEMS). Samples prepared with and without applied stress were annealed at high temperatures. Fig. 7 compares CEMS pattern of a sample prepared with and without applied stress before and after annealing at 473 K. The CEMS patterns were fitted assuming a sextate due to Fe nanocrystals and a doublet due to amorphous phase. Even in the as-deposited state a sextate with hyperfine

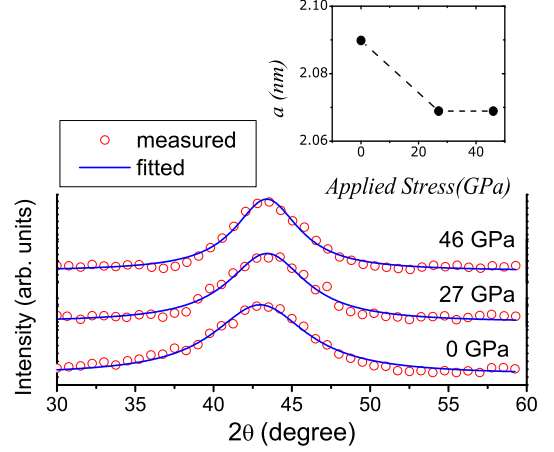


FIG. 4: (color online) X-ray diffraction pattern of the isotopic multilayers in the as-deposited state. The measurements were carried out in the grazing incidence geometry using  $\text{Cu-K}\alpha$  x-rays. The inset in the figure shows the change in inter-atomic distance as a function of annealing temperature.

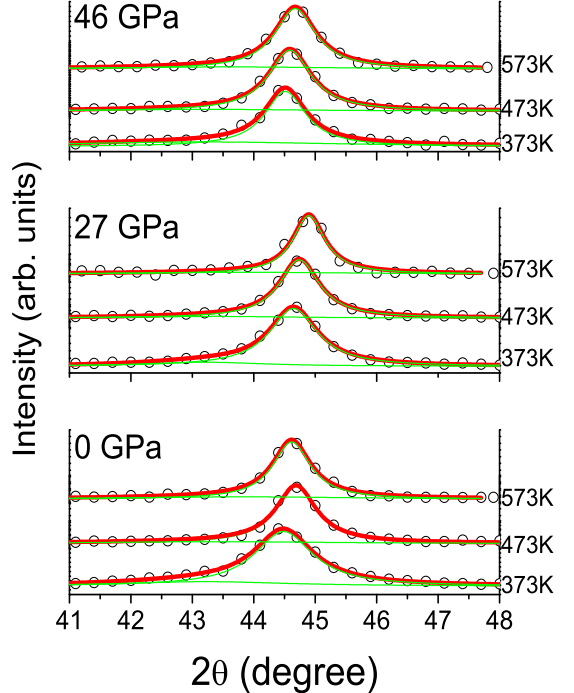


FIG. 5: (color online) Grazing incidence x-ray diffraction pattern of  $\text{Si}/[\text{natural Fe}_{75}\text{Zr}_{25} (25\pm 1 \text{ nm})/^{57}\text{Fe}_{75}\text{Zr}_{25}(12\pm 1 \text{ nm})]_{10}$  multilayer prepared with an applied stress of 0, 27 and 46 GPa after annealing at different temperatures. Open circles represent the measured data and the solid lines are fit to them.

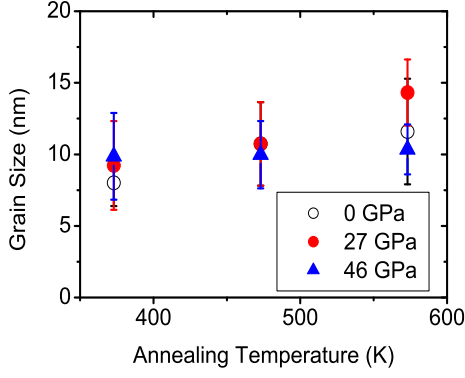


FIG. 6: (color online) Average grain size as a function of annealing temperature shown representatively for a sample prepared with an applied stress of 0, 27 and 46 GPa.

field of about 10 Tesla was found to be present. However, the area ratio of this sextate is very small. This indicates that there is a small amount of magnetic alloy while most of the alloy is not ferromagnetic. As the samples were annealed the contribution of this magnetic phase increases indicating an enhancement in the volume fraction of nanocrystalline Fe in agreement with the XRD results. It may be noted that the hyperfine field after annealing remains in the range of 18-23 Tesla while that of pure Fe is 33.3 Tesla. The reduced magnetic moment could result due to some thermal fluctuations. Table I compares the fitted values for the different cases as shown in fig. 7.

TABLE I: Fitted CEMS parameters for the sample prepared with and without an applied stress in the as-deposited state and after annealing at 473 K.

Sample	Sample Condition	Average Hyperfine Field (T)	Average Quadrupole ( $\text{mm s}^{-1}$ )
0 GPa	As-deposited	$10.8 \pm 0.5$ T	$0.40 \pm 0.01$
0 GPa	473 K, 1 hour	$18.4 \pm 1.3$ T	$0.43 \pm 0.01$
27 GPa	As-deposited	$10.2 \pm 0.9$ T	$0.44 \pm 0.01$
27 GPa	473 K, 1 hour	$23.4 \pm 0.8$ T	$0.70 \pm 0.01$
46 GPa	As-deposited	$13.0 \pm 0.2$ T	$0.44 \pm 0.01$
46 GPa	473 K, 1 hour	$22.5 \pm 1.5$ T	$0.42 \pm 0.01$

MOKE measurements were also performed to understand the changes in the magnetic properties of the system during amorphous to nanocomposite phases. The sample prepared without an applied stress exhibited no anisotropy as a function of azimuthal angle in the coercivity. While the samples prepared with an applied stress clearly show uniaxial anisotropy, which persists even after the nanocrystallization of the films (see fig. 8). This confirms that the bending stress induced in the films persists even after nanocrystallization.

Formation of a nano-composite phase after primary crystallization of the amorphous phase is a general phe-

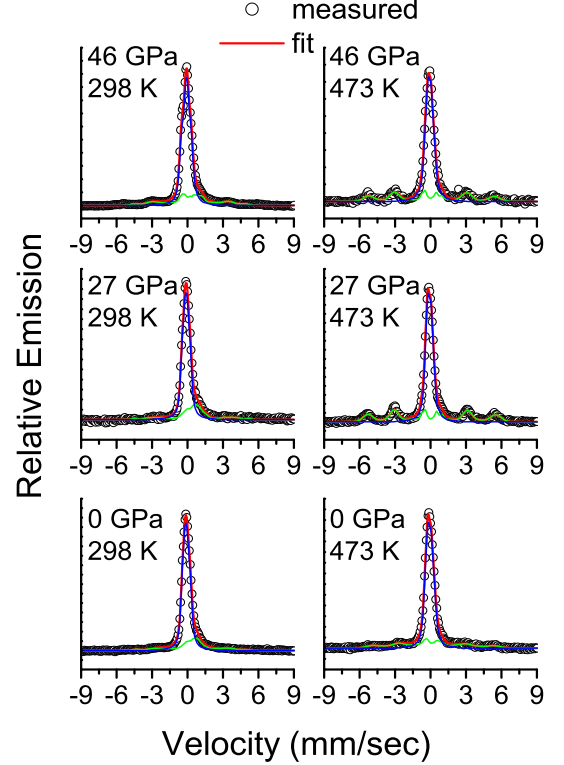


FIG. 7: (color online) Conversion electron Mössbauer spectroscopy (CEMS) pattern of  $\text{Si}/[^{\text{natural}}\text{Fe}_{75}\text{Zr}_{25} (25 \pm 1 \text{ nm})]/[^{57}\text{Fe}_{75}\text{Zr}_{25} (12 \pm 1 \text{ nm})]_{10}$  multilayer prepared with an applied stress of 0, 27 and 46 GPa in the as-deposited state and after annealing at 473 K.

nomenon in amorphous alloys. Often, it was observed that amorphous binary alloys crystallize in two steps. The primary crystallization reaction of most of amorphous alloys leads to an evolution of nanocrystalline microstructures whereas the phase formed after the second stage results in an intermetallic compound along with the nanocrystalline phase. The nominal reaction for such crystallization process had been given as: amorphous  $\rightarrow \alpha + \text{amorphous} \rightarrow \alpha + \beta$ ; where  $\alpha$  is the primary phase that precipitates out from the amorphous matrix and  $\beta$  is an intermetallic compound.<sup>2,11,12</sup> In the present case crystallization of the amorphous phase can be regarded as the primary crystallization process and as evident from the x-ray data, the amorphous phase co-exists along with grains of  $\alpha$ -Fe. However, the primary crystallization temperature for the present case was found to be very low as compared with  $\text{Fe}_{67}\text{Zr}_{33}$  amorphous alloy.<sup>21</sup> Since in the present case for  $\text{Fe}_{75}\text{Zr}_{25}$  alloy, the Zr content is slightly lower, a decrease in crystallization temperature is not very surprising. In order to further confirm the structure of the alloy, a thin film with even lower Zr content was deposited under identical conditions of sputtering.<sup>27</sup> The composition of this film was  $\text{Fe}_{80}\text{Zr}_{20}$ . The XRD pattern

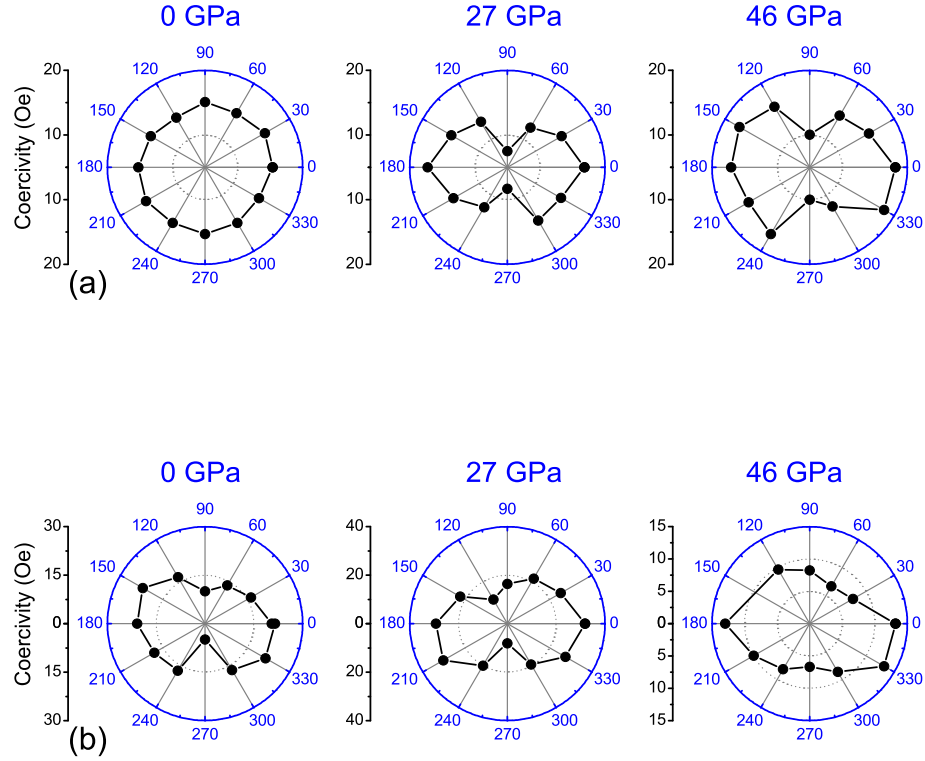


FIG. 8: (Color online) MOKE measurements on  $\text{Si}/[\text{naturalFe}_{75}\text{Zr}_{25} (25\pm 1 \text{ nm})/\text{}^{57}\text{Fe}_{75}\text{Zr}_{25}(12\pm 1 \text{ nm})]_{10}$  multilayer prepared with an applied stress of 0, 27 and 46 GPa in the as-deposited state (a) and after annealing at 473 K (b).

of this film showed a narrow peak even in the as-prepared state (not shown in the figure), indicating that the structure forms a nanocrystalline state. Such a decrease in the primary crystallization temperature was also observed in an ion beam sputtered  $\text{Fe}_{85}\text{Zr}_{15}$  sample,<sup>28,29</sup> and a phenomenon analogue to surface crystallization in amorphous alloy ribbons<sup>30,31,32,33</sup> was found responsible for early crystallization of amorphous  $\text{Fe}_{85}\text{Zr}_{15}$  film in the thin film state.

For the amorphous thin film formed by vapor deposition, the effective quenching rate is very high which results in a higher quenched-in free volume and results in an early crystallization of the amorphous phase as observed in the present case. In order to further understand the crystallization behavior of the alloy, DSC measurements were carried out under a constant heating rate of 0.33 K/s. It was found that a very broad hump appears around 450 K and a relatively sharp peak appears around 613 K in all the three samples. The hump appearing at 450 K can be estimated as first crystallization step while relatively sharp peak corresponds to second crystallization step. From the XRD results, the first crystallization event was observed as early as 373 K, where the samples were annealed for 1 hour, in the DSC scan since the samples were heated at a much faster rate, the crystalliza-

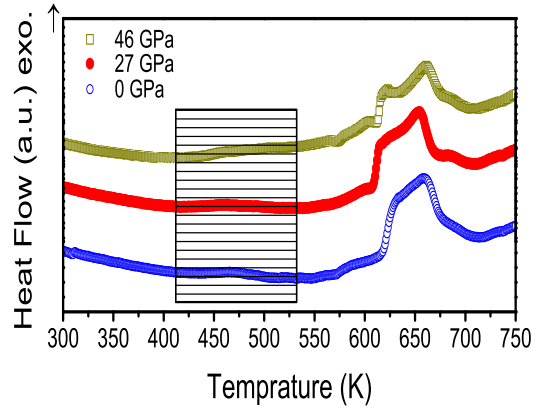


FIG. 9: (color online) DSC scans of the  $\text{Si}/[\text{naturalFe}_{75}\text{Zr}_{25} (25\pm 1 \text{ nm})/\text{}^{57}\text{Fe}_{75}\text{Zr}_{25}(12\pm 1 \text{ nm})]_{10}$  multilayer prepared with an applied stress of 0, 27 and 46 GPa. The shaded region shown in the figure corresponds to the temperature range used for diffusion measurements.



tion event was observed at higher temperature as shown in fig. 9. In a number of studies performed on bulk or thick films (thickness few  $\mu\text{m}$ ), it has been found that the heat release during the first crystallization event is significantly smaller compared to the second crystallization event due to a slower diffusion at lower temperature.<sup>34</sup> In Al-based glasses, Foley et al<sup>35</sup> have studied the crystallization behavior using transmission electron microscopy (TEM) and DSC. While growth of nanocrystals was confirmed by TEM, there was no evidence of primary crystallization with DSC. Small diffusion of the constituents was argued for the observed behavior. In their case, they observed that, for diffusivity,  $D \sim 1 \times 10^{-19} \text{ m}^2\text{s}^{-1}$ , the level of heat output is nearly undetectable in DSC measurements, which requires a signal on the order of 0.1 mW or greater. Unless the value of  $D$  was at least two orders of magnitude larger, the signal will be close to the noise level of the DSC. It may be noted that in the present case, the iron self-diffusivity around 400 K, is of the order of  $10^{-21} \text{ m}^2\text{s}^{-1}$  (as shown in later sections). Further, the grain-size as determined with XRD results was about 10 nm, the heat release for the formation of small grain sizes is expected to be small. In addition, the DSC measurements in the present case were performed in relatively thin film (370 nm) and the total mass exposed during DSC measurements was only 65  $\mu\text{gm}$  which explains small heat release during the first crystallization event, in spite of the high sensitivity of the sensor used during DSC measurements. The presence of peak around 613 K, can be understood as second crystallization step. The onset of second crystallization temperature was found around  $(608 \pm 5) \text{ K}$  for all the 3 samples and there was no systematic effect of applied stress on the second crystallization temperature.

### C. Self-Diffusion Measurements - Time Dependence

With the observed thermal behavior of the samples, for diffusion measurements, a temperature range for diffusion annealing was chosen from 413-533 K in order to study diffusion in the nano-composite state. This temperature region is also indicated in fig. 8 as shaded area. The three samples prepared with an applied compressive stress of 0, 27 and 46 GPa were first pre-annealed at 373 K for 0.5 hour to obtain the nano-composite phase. For studying the time dependence of diffusivity, the samples were further annealed at 473 K and neutron reflectivity measurements were carried out after each annealing. In order to minimize the fluctuations due to a possible variation in the temperature, all the samples were annealed simultaneously in the furnace. Fig. 10 shows a plot of neutron reflectivities as a function of annealing time at 473 K. A relatively small time step was chosen in order to observe the structural relaxation of the samples. As can be seen from the figure, after annealing, the intensity at the Bragg peak decays. The initial decay was

found to be much faster as compared to that with later annealing time. The decay of the Bragg peak intensity can be used to calculate the diffusion coefficient using the expression<sup>36</sup>:

$$\ln[I(t)/I(0)] = -8\pi^2 n^2 D(T)t/d^2, \quad (3)$$

where  $I(0)$  is the intensity before annealing and  $I(t)$  is the intensity after annealing time  $t$  at temperature  $T$ . The diffusion length  $L_d$  is related to diffusivity through the relation:

$$L_d = \sqrt{2D(T)t}, \quad (4)$$

where  $t$  is the annealing time. The height of the Bragg peak was determined after subtracting the background due to Fresnel reflectivity by multiplying the data by a factor of  $q^4$ , where  $q$  is the momentum transfer. Fig. 11 shows an evolution of the diffusion length as a function of annealing time at 473 K. As can be seen from the figure, the diffusion lengths below an annealing time of 600 s were found to increase much faster as compared to later annealing times. Such behavior in evolution of the diffusion length was also observed for  $\text{Fe}_{67}\text{Zr}_{33}$  amorphous sample<sup>21</sup> and is a direct consequence of structural relaxation in the structures.<sup>37,38</sup>

It is interesting to see that for the sample prepared without any stress, the diffusion length increased much faster as compared to the samples prepared with an applied stress. As it is evident from the structural and magnetic measurements, samples prepared with an applied stress exhibited a more relaxed state as compared to that obtained without an applied stress. It is expected that structural relaxation would be more dominant for the sample prepared without an applied stress. The overall magnitude of the diffusion length follows the strength of applied stress and the degree of relaxation is proportional.

### D. Self-Diffusion Measurements - Temperature Dependence

In order to measure the activation energy for diffusion, the samples were annealed in the temperature range of 413-533 K with a step of 40 K. As can be seen from the fig. 11, after an annealing time of 1800 s, in all cases, the fast relaxation process was almost completed, therefore for the calculation of the activation energy of the system all the samples were annealed for 1800 s at the above mentioned temperatures. It may be noted that annealing for 1800 s may not produce a fully relaxed state of the structure, even though for a comparison of diffusivities for the samples prepared with different applied stress, the time for diffusion annealing was kept constant.

Fig. 12 shows the neutron reflectivity pattern obtained after annealing at different temperatures. Again in order to minimize a possible fluctuation in the temperature

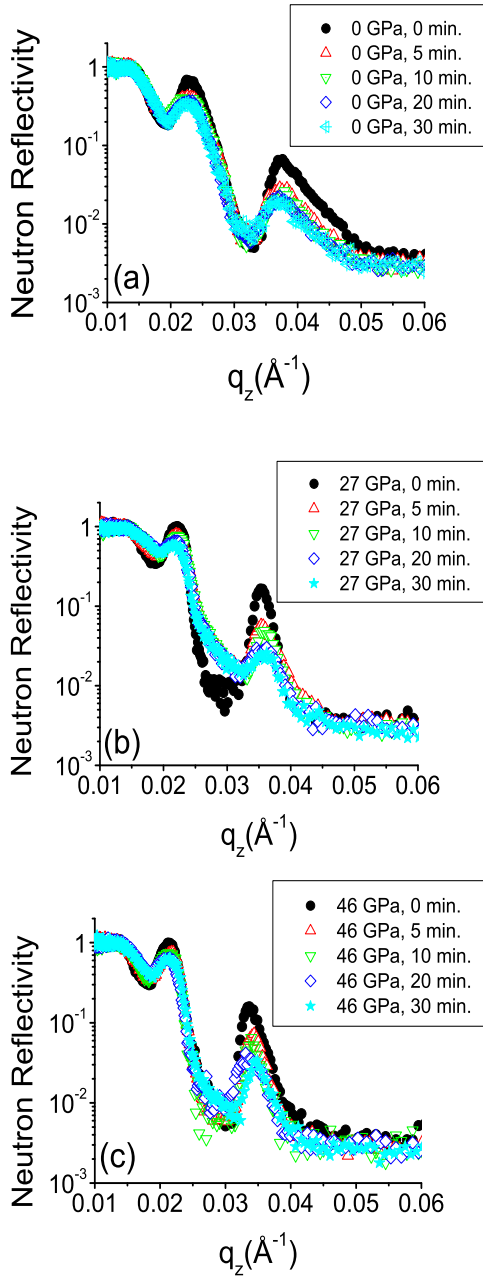


FIG. 10: (color online) Decay of the Bragg peak intensity as a function of annealing time at 473 K for the sample prepared without an applied stress (a) with an applied stress of 27 GPa (b) and with an applied stress of 46 GPa (c).

and annealing conditions, all the three samples were annealed simultaneously in the furnace. For a comparison, the neutron reflectivity pattern in the as-prepared state is also shown in the figure. As evident from XRD and CEMS measurements, after annealing the samples undergo from the amorphous to the nano-composite state, the intensity at the Bragg peaks increases marginally in the neutron reflectivity patterns. In a previous study, it was observed that at the event of primary crystallization in the amorphous  $\text{Fe}_{67}\text{Zr}_{33}$  alloy<sup>21</sup> the neutron reflectivity pattern of an  $[\text{natural}\text{Fe}_{67}\text{Zr}_{33}(9\text{ nm})\text{ }^{57}\text{Fe}_{67}\text{Zr}_{33}(5$

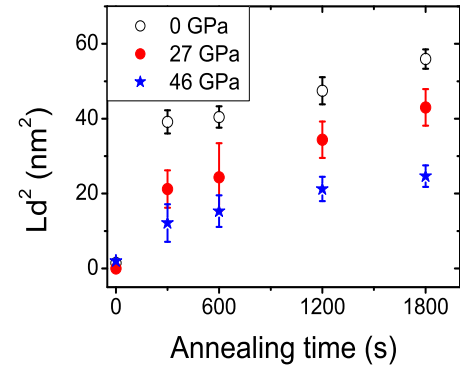


FIG. 11: (color online) Evolution of diffusion length as a function of annealing time and applied stress at 473 K in nanocomposite  $\text{Si}/[\text{natural}\text{Fe}_{75}\text{Zr}_{25}(25\pm 1\text{ nm})/^{57}\text{Fe}_{75}\text{Zr}_{25}(12\pm 1\text{ nm})]_{10}$ .

$\text{nm})]_{20}$  multilayer, showed an increase in the intensity at the Bragg peak by a factor as high as 10, as compared to the as-deposited sample. Also the x-ray reflectivity pattern showed an appearance of a Bragg peak due to crystallization accompanied by a phase separation in the alloy.<sup>21</sup> In the present case however, after annealing at 373 K, the amorphous phase nanocrystallize, but the intensity at the Bragg peak increases only marginally ( $<10\%$ ). Also as shown in the fig. 13, no Bragg peak or structure due to a chemical period appeared up to 573 K in the XRR pattern. This indicates that the primary crystallization behavior of  $\text{Fe}_{75}\text{Zr}_{25}$  alloy is different as compared to that of previously studied  $\text{Fe}_{67}\text{Zr}_{33}$  alloy.<sup>21</sup> However, since the matrix obtained after nanocrystallization showed no further significant changes between the temperature range 373-575 K (see also fig. 8), it is expected that the diffusion process would be not interfered by structural changes. As shown in fig. 12, the intensity at both the Bragg peaks decreases with increase in annealing temperature and after annealing at 533 K, the Bragg peak intensity almost vanishes. This indicates that after annealing at 533 K, both the natural and  $^{57}\text{Fe}$  are layers almost completely diffused. With the procedure discussed in the previous section, the diffusivity at each temperature was obtained. Fig. 14 shows a plot of diffusivities obtained with both the Bragg peaks for the three samples. As can be seen from the figure, both the Bragg peaks yield similar diffusivities within the experimental errors. The error bars in the present case are basically representing the errors in determining the height of the Bragg peaks obtained from a peak fitting procedure.

The values for the diffusivity obtained for the three samples at the abovementioned temperatures (along with the separately annealed samples at 473 K), could be fitted to the relation,  $\ln D = \ln D_0 - (E/k_B T)$ , where  $D_0$ ,  $E$  and  $T$  are the pre-exponential factor, the activation energy and the annealing temperature respectively and  $k_B$  is the Boltzmann constant. In all the three cases the logarithm of diffusivity follows Arrhenius behavior and accordingly,



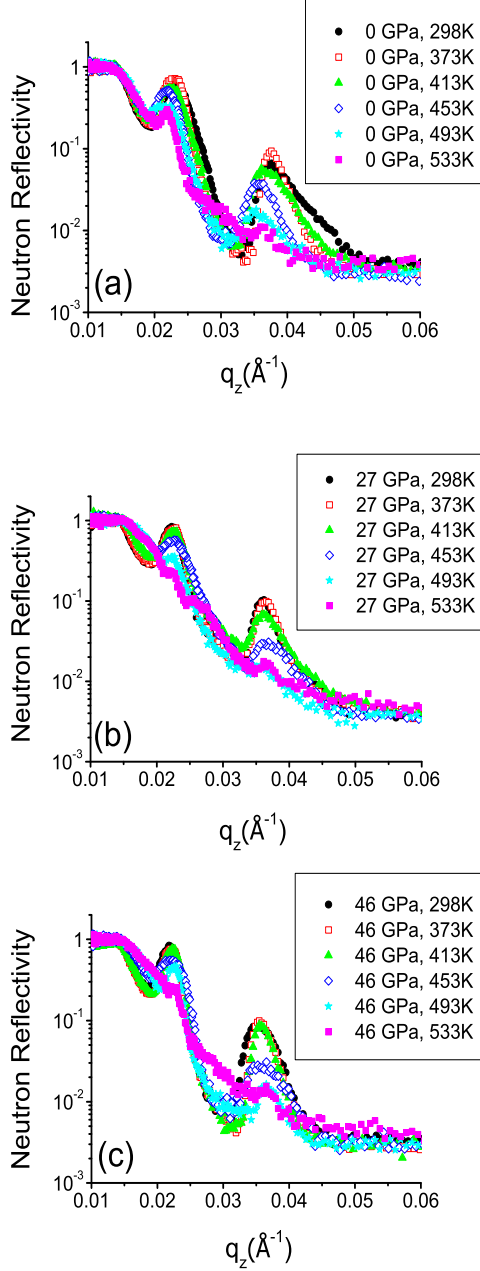


FIG. 12: (color online) Decay of the Bragg peak intensity as a function of annealing temperature for the sample prepared without an applied stress (a) with an applied stress of 27 GPa (b) and with an applied stress of 46 GPa (c).

the activation energy and the pre-exponential factor for iron self-diffusion in  $\text{Fe}_{75}\text{Zr}_{25}$  alloy was obtained. The observed values of both the  $E$  and  $D_0$  are given in table II along with the values obtained for amorphous  $\text{Fe}_{67}\text{Zr}_{33}$  alloy. Fig. 15 shows a plot of diffusivities obtained from the 1st order Bragg peak for the sample at 0, 27 and 46 GPa. The activation energy was found to increase with an increase in the strength of applied compressive stress (a steeper slope was observed with an increase in the

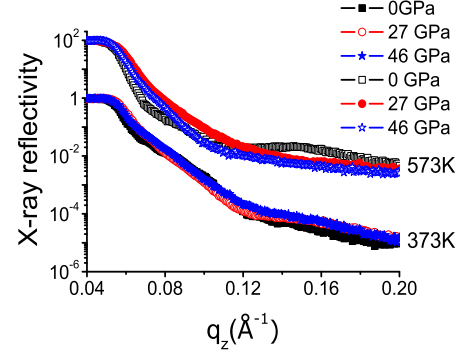


FIG. 13: (color online) X-ray reflectivity pattern of the  $\text{Si}/[^{\text{natural}}\text{Fe}_{75}\text{Zr}_{25} (25\pm 1 \text{ nm})/^{57}\text{Fe}_{75}\text{Zr}_{25} (12\pm 1 \text{ nm})]_{10}$  multilayers prepared with and without applied stress after annealing at 373 and 473 K

TABLE II: Activation energy and the pre-exponential factor for iron self-diffusion in nanocrystalline  $\text{Si}/[^{\text{natural}}\text{Fe}_{75}\text{Zr}_{25} (25\pm 1 \text{ nm})/^{57}\text{Fe}_{75}\text{Zr}_{25} (12\pm 1 \text{ nm})]_{10}$  multilayers as a function of applied stress during sample preparation. Both the activation energy and the pre-factor represent the statistical averaged values obtained from the 1st and 2nd order Bragg peaks.

Sample	Sample condition	Activation energy (E, eV)	Prefactor ( $D_0$ , $\text{m}^2\text{s}^{-1}$ )
nano.- $\text{Fe}_{75}\text{Zr}_{25}$	0 GPa	$0.24\pm 0.05$	$3\times 10^{-18\pm 1}$
nano.- $\text{Fe}_{75}\text{Zr}_{25}$	27 GPa	$0.31\pm 0.05$	$1\times 10^{-17\pm 1}$
nano.- $\text{Fe}_{75}\text{Zr}_{25}$	46 GPa	$0.51\pm 0.05$	$1\times 10^{-15\pm 1}$
amorphous- $\text{Fe}_{67}\text{Zr}_{33}$	0 GPa	$0.38\pm 0.05$	$3\times 10^{-18\pm 1}$

applied stress). The result gives a clear indication that diffusivity for the sample prepared with applied stress is much slower as compared with that prepared without an applied stress. This result also supports the time dependence of the diffusivity as shown in fig. 11.

In an earlier study Klugkist et al<sup>39,40</sup> studied Co and Zr self-diffusion in amorphous CoZr alloy using Radioactive tracer method as a function of pressure and temperature dependence. It was found that the pressure dependence for Co self-diffusion is extremely small while for Zr self-diffusion it is of the order of one activation volume. On the basis of obtained results it was concluded that Zr diffuses via thermal defects, whereas vacancy like thermal defects can be ruled out for Co self-diffusion. However, our results clearly indicates a decrease in diffusivity with an increase in applied stress. Here we would like to point out that a direct comparison between the studies performed earlier<sup>39,40</sup> with that of our results could not be made. The following points are important to understand our results (i) The neutron reflectometry technique offers a depth resolution in sub nano meter range it is possible to measure initial stage of self-diffusion in a alloy unlike

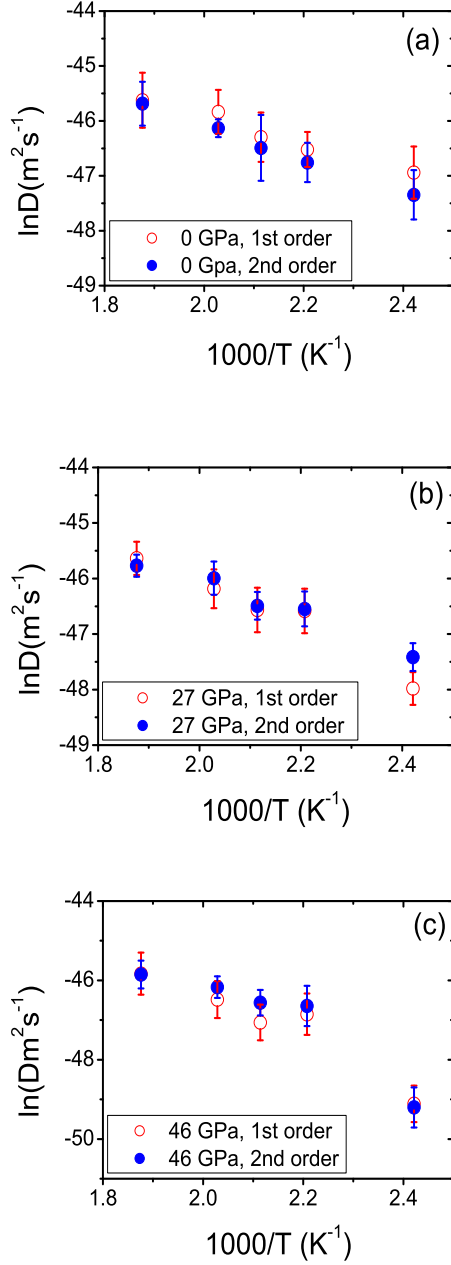


FIG. 14: (color online) Arrhenius behavior of the diffusivity obtained from the 1st and 2nd order Bragg peaks for samples prepared with an applied stress of 0 GPa (a), 27 GPa (b) and 46 GPa (c).

conventional techniques e.g. SIMS or radioactive tracer method (ii) As mentioned already that in our case, the alloy could have not attained a fully relaxed state as pre-annealing time was very short compared with that in literature. Combining the above mentioned points, it is not surprising that there is a strong dependence of self-diffusion of Fe on applied stress, which points out that in the initial state the diffusion mechanism could be different.

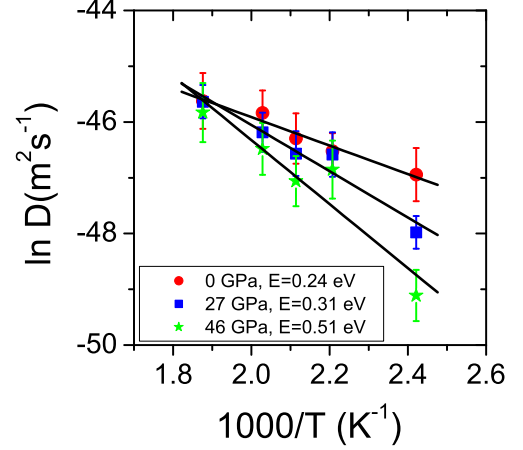


FIG. 15: (color online) Activation energy and pre-exponential factor for diffusion as a function of applied stress in  $\text{Si}/[^{\text{natural}}\text{Fe}_{75}\text{Zr}_{25} (25 \pm 1 \text{ nm})/^{57}\text{Fe}_{75}\text{Zr}_{25} (12 \pm 1 \text{ nm})]_{10}$  multilayer. The data corresponds to the diffusivity obtained from the 1st order Bragg peak. The sample prepared with the highest applied gives and activation energy more than twice as compared with the sample prepared without an applied stress. The detailed values of activation energy and the pre-exponential factors are given in table II.

Comparing the diffusivity for the sample prepared at 0 GPa with that of amorphous  $\text{Fe}_{67}\text{Zr}_{33}$  sample (also prepared at 0 GPa), the diffusivity in the nano-composite state is slightly higher as compared to the amorphous sample. The activation energy for the nanocomposite sample was lower by 0.14 eV, while the pre-exponential factors were found to be exactly similar (see table II). An enhancement in diffusivity in the nano-composite state is not unexpected due to presence of grains and grain-boundaries (GB), while the amorphous phase is expected to be free from grains and GBs. However the enhancement in diffusivity in the present case is not as spectacular as observed e.g. in the FINEMET type nanocrystalline- $\text{Fe}_{73.5}\text{Si}_{13.5}\text{B}_9\text{Nb}_3\text{Cu}_1$  in which the Fe self-diffusion showed a large enhancement over that in the parent amorphous phase.<sup>41,42</sup> It may be noted that in the present case the composition of the nano-composite  $\text{Fe}_{75}\text{Zr}_{25}$  alloy is also not similar to the amorphous  $\text{Fe}_{67}\text{Zr}_{33}$  alloy, therefore an enhancement in diffusivity may also occur due to increased concentration of Fe. In another study self-diffusion of iron was measured in the parent amorphous and nano-composite  $\text{Fe}_{85}\text{Zr}_{15}$  alloy thin film produced by ion-beam sputtering. It was found that iron self-diffusion in both amorphous and nano-composite state was similar and found to occur exclusively through the GB regions which were amorphous in nature.<sup>28</sup> In the present case as well the GBs in the nano-composite state are amorphous, which might happen due to the fact that in the nano-composite state, the structure consists of a mixture of nanocrystalline grains

of Fe and remaining amorphous phase. The nanocrystalline grains of Fe would be surrounded by amorphous GBs and in such a situation a percolating path between the nanocrystals may not establish and diffusivity in the nano-composite phase would be similar to that in the amorphous state.

On the other hand, the activation energy obtained for the sample prepared with highest applied stress was found to be larger (slower diffusivity) as compared to the amorphous Fe<sub>67</sub>Zr<sub>33</sub> sample. This is somewhat surprising as the sample prepared even at the highest stress is also in the nano-composite state. In case the diffusion mechanism is dominated by grains and GBs the effective applied stress should result in an enhancement of the diffusivity.<sup>43</sup> As discussed earlier, an applied compressive stress produced a more relaxed state of the sample as compared to samples prepared without stress. If the diffusion mechanism is dominated by a somewhat collective type migration of atoms both in amorphous and nano-composite case, annihilation of free volume would result into a diffusion mechanism involving a small group of atoms.

#### IV. CONCLUSIONS

In the present work, the effect of compressive stress on self-diffusion of iron in chemically homogenous multilayers of FeZr/<sup>57</sup>FeZr was investigated. It was found that samples in the as-prepared state were amorphous and undergo primary crystallization when annealed at 373 K. The diffusion measurements were performed in the nano-composite state and it was observed that with an increase in the strength of applied stress, the diffusivity decreases as compared to the sample prepared without an applied stress. An applied compressive stress on to the multilayer produced a more relaxed state of the sample as seen from XRD. A diffusion mechanism involving a small group of atoms explains the observed diffusivity in the chemically homogeneous multilayers.

#### V. ACKNOWLEDGEMENT

Authors would like to acknowledge: A. Foelske, General Energy Research, Paul Scherrer Institute, for providing help in x-ray photoelectron spectroscopy measurements, K. Conder, P. Keller, and M. Horisberger, Laboratory for Neutron Scattering, Paul Scherrer Institute for providing help in DSC measurements, manufacturing of 3-point Si wafer bending machine, assisting in thin film deposition, respectively. This work was performed at the Swiss Spallation Neutron Source, Paul Scherrer Institute, Villigen, Switzerland.

- 
- \* Electronic address: mgupta@csr.ernet.in
- <sup>1</sup> P. G. Debenedetti and F. H. Stillinger, *Nature* **410**, 259 (2001).
  - <sup>2</sup> C. A. Angell, K. L. Ngai, G. B. McKenna, P. F. McMillan, and S. Martin, *J. Appl. Phys.* **88**, 3113 (2000).
  - <sup>3</sup> M. E. McHenry, M. A. Willard, and D. E. Laughlin, *Prog. Mat. Sci.* **44**, 291 (1999).
  - <sup>4</sup> A. Dunlop, G. Jaskierowicz, G. Rizza, and M. Kopcewicz, *Phys. Rev. Lett.* **90**, 015503 (2003).
  - <sup>5</sup> E. Ma, *Nature materials* **2**, 7 (2002).
  - <sup>6</sup> A. Kojima, A. Makino, and A. Inoue, *J. Appl. Phys.* **87**, 6576 (2000).
  - <sup>7</sup> A. Kojima, F. Ogiwara, A. Makino, A. Inoue, and T. Masumoto, *Mater. Sci. Eng. A* **226-228**, 520 (1997).
  - <sup>8</sup> X. Y. Zhang, Y. Guan, J. W. Zhang, W. Sprengel, K. J. Reichle, K. Blaurock, K. Reimann, and H.-E. Schaefer, *Phys. Rev. B* **66**, 212103 (2002).
  - <sup>9</sup> B. B. Kappes, B. E. Meacham, Y. L. Tang, and D. J. Branagan, *Nanotechnology* **14**, 1228 (2003).
  - <sup>10</sup> W. J. Botta, F. D. Negri, and A. R. Yavari, *J. Non-Cryst. Solid* **247**, 19 (1999).
  - <sup>11</sup> K. Hono and D. H. Ping, *Materials Characterization* **44**, 203 (2000).
  - <sup>12</sup> D. M. Zhu, K. Raviprasad, K. Suzuki, and S. P. Ringer, *J. Phys. D : Appl. Phys.* **37**, 645 (2004).
  - <sup>13</sup> Y. Yoshizawa, S. Oguma, and K. Yamauchi, *J. Appl. Phys.* **64**, 6044 (1988).
  - <sup>14</sup> K. Suzuki, A. Makino, N. Kataika, A. Inoue, and T. Masumoto, *Mater. Trans. JIM* **32**, 93 (1991).
  - <sup>15</sup> M. A. Willard, M.-Q. Huang, D. E. Laughlin, M. E. McHenry, J. O. Cross, V. G. Harris, and C. Franchetti, *J. Appl. Phys.* **85**, 4421 (1999).
  - <sup>16</sup> F. Faupel, W. Frank, M. P. Macht, H. Mehrer, K. Rätzke, H. R. Schober, S. K. Sharma, and H. Teichler, *Rev. Mod. Phys.* **75**, 237 (2003).
  - <sup>17</sup> R. Abermann and R. Koch, *Thin Solid Films* **129**, 71 (1985).
  - <sup>18</sup> A. L. Shull and F. Spaepen, *J. Appl. Phys.* **80**, 6243 (1996).
  - <sup>19</sup> J. Floro, S. J. Hearne, J. A. Hunter, P. Kotula, E. Chason, S. C. Seel, and C. V. Thompson, *J. Appl. Phys.* **89**, 4886 (2001).
  - <sup>20</sup> R. Koch, *J. Phys.: Condens. Matter* **6**, 9519 (1994).
  - <sup>21</sup> M. Gupta, A. Gupta, J. Stahn, M. Horisberger, T. Gutberlet, and P. Allenspach, *Phys. Rev. B* **70**, 184206 (2004).
  - <sup>22</sup> G. G. Stoney, *Proc. R. Soc. A* **82**, 172 (1909).
  - <sup>23</sup> J. Chen and I. D. Wolf, *Semicond. Sci. Technol.* **18**, 261 (2003).
  - <sup>24</sup> M. Gupta, T. Gutberlet, J. Stahn, P. Keller, and D. Clemens, *Pramana J. Phys.* **63**, 57 (2004).
  - <sup>25</sup> L. Parratt, *Phys. Rev.* **95**, 359 (1954).
  - <sup>26</sup> A. Guinier, *X-Ray Diffraction : In Crystals, Imperfect Crystals and Amorphous Bodies* (Dover, New York, 1994).
  - <sup>27</sup> M. Gupta, R. Gupta, A. Gupta, and T. Gutberlet (Unpublished).
  - <sup>28</sup> A. Gupta, M. Gupta, U. Pietsch, S. Ayachit, S. Rajagopalan, A. K. Balamurgan, and A. K. Tyagi, *J. Non-Cryst. Solids* **343**, 39 (2004).
  - <sup>29</sup> M. Gupta and A. Gupta, *Phys. Status. Solidi C* **1**, 3211

- (2004).
- <sup>30</sup> A. Gupta, S. Habibi, S. Lal, and G. Principi, *Hyperfine Interaction* **55**, 967 (1990).
  - <sup>31</sup> A. P. Radlinski and A. Calka, *Phys. Rev. Lett.* **57**, 3081 (1986).
  - <sup>32</sup> P. R. Rao, *Rev. Solid State Sci.* **3**, 311 (1989).
  - <sup>33</sup> U. Köster and B. Punge-Witteler, *Mat. Res. Soc. Symp. Proc.* **80**, 355 (1987).
  - <sup>34</sup> J. H. Perepezko, R. J. Hebert, R. I. Wu, and G. Wilde, *J. Non-Cryst. Sol.* **317**, 52 (2003).
  - <sup>35</sup> J. C. Foley, D. R. Allen, and J. H. Perepezko, *Scripta Materialia* **35**, 655 (1996).
  - <sup>36</sup> J. Speakman, P. Rose, J. A. Hunt, N. Cowlam, R. E. Somekh, and A. L. Greer, *J. Magn. Magn. Mat.* **156**, 411 (1996).
  - <sup>37</sup> Y. Loirat, J. L. Boequet, and Y. Limoge, *J. Non-Cryst. Solids* **265**, 252 (2000).
  - <sup>38</sup> M. Gupta, A. Gupta, S. Rajagopalan, and A. K. Tyagi, *Phys. Rev. B* **65**, 214204 (2002).
  - <sup>39</sup> P. Klugkist, K. Rätzke, S. Rehders, P. Torche, and F. Faupel, *Phys. Rev. Lett.* **80**, 3288 (1998).
  - <sup>40</sup> P. Klugkist, K. Rätzke, and F. Faupel, *Phys. Rev. Lett.* **81**, 614 (1998).
  - <sup>41</sup> H. Tanimoto, P. Farber, R. Würschum, R. Z. Valiev, and H. E. Schaefer, *Nanostruct. Mater.* **12**, 681 (1999).
  - <sup>42</sup> R. Würschum, P. Farber, R. Dittmar, P. Scharwaechter, W. Frank, and H.-E. Schaefer, *Phys. Rev. Lett.* **79**, 4918 (1997).
  - <sup>43</sup> K. M. Crosby, *cond-mat/0307065*.